Supplementary Information (SI) for Chemical Science.
This journal is © The Royal Society of Chemistry 2026

Supporting Information for

Low-Valent Mo Single Atoms Stabilized by Electronegative Oxygen Coordination Enables Efficient Water Oxidation

Yang Yang, [*, †] *Ji-Kai Li,* [†] *Qian-Nan Yang,* [†] *Yi-Bin Yang,* [*, ‡] *Jian-Hua Meng,* [†] *Lin Zhang,* [Γ] *Ying-Dan Wu,* [†] *Ke-Xiang Wang,* [†] *Huan Chen,* [†] *Zhi-Yuan Jiang,* [†] *Rui Chao,* [†] *Wei-Tao Wang,* [†] *Xiao Ma,* [*, Γ] *and Zhao-Tie Liu* [*, #]

[†]*Key Laboratory of Chemical Additives for China National Light Industry, College of Chemistry and Chemical Engineering, Shaanxi University of Science and Technology, Xi'an, 710021, China*

[‡]*Chemical Pollution Control Chongqing Applied Technology Extension Center of Higher Vocational Colleges, Chongqing Industry Polytechnic University, Chongqing, 401120, China*

[Γ]*State Key Laboratory of Solidification Processing, School of Materials Science and Engineering, Northwestern Polytechnical University, YouyiXi Road 127, Xi'an 710072, China*

[#]*School of Chemistry and Chemical Engineering, Shaanxi Normal University, Xi'an, 710119, China*

Corresponding Authors

*E-mail: yyang399@sust.edu.cn (Y. Yang); yangyb@cqipu.edu.cn (Y.-B. Yang); maxiaonpu@nwpu.edu.cn (X. Ma); ztliu@snnu.edu.cn (Z.-T. Liu).

Contents

1. Experimental Section

1.1. Synthesis of Catalysts

1.1.1. Pretreatment of nickel foam (NF)

Prior to use, nickel foam (1 cm × 4 cm, thickness ~1.5 mm, Kunshan Lvchuang Electronic Technology) underwent sequential pretreatment. First, both sides were plasma-treated for 10 min under high-purity O_2 (99.999%) atmosphere at 150 W power using a PECVD system (OTF-1200X-80-II-4CV-PE-SL, Hefei Kejing Materials Technology Corporation). Subsequently, the foam was subjected to ultrasonic cleaning (10 min each) in 1 M HCl, acetone, ethanol, and ultrapure water, followed by N_2 drying.

1.1.2. Synthesis of NiFe layered double hydroxide (LDH) powders

The precursor solution was prepared by dissolving 348.9 mg of $Ni(NO_3)_2 \cdot 6H_2O$ (98%, Alfa), 79.5 mg of $FeCl_2 \cdot 4H_2O$ (99.95%, Macklin), and 296 mg of NH_4F (98%, Aladdin) in 40 mL ultrapure water (18.2 MΩ cm), forming a pea-green solution. Subsequently, 480.5 mg urea (99%, Aladdin) was added under vigorous stirring until complete dissolution. 15 mL of the homogeneous solution was then transferred to a 25 mL Teflon-lined stainless-steel autoclave and subjected to hydrothermal treatment at 120 ℃ for 6 h. After natural cooling to 25 ℃, the resulting product was collected by centrifugation (4000 rpm, 5 min). The obtained precipitate was thoroughly wash with ultrapure water and ethanol (99.7%, Sinopharm) through at least three centrifugation cycles, followed by drying at 60 ℃ for 12 h.

1.1.3. Synthesis of NiFe LDH grown on nickel foam (NiFe LDH@NF)

NiFe LDH was grown *in situ* on pretreated nickel foam (NiFe LDH@NF) through a

modified hydrothermal process. A piece of plasma-treated nickel foam was immersed in 15 mL of the precursor solution (prepared as described above) within a 25 mL Teflon-lined autoclave. Following identical hydrothermal conditions (120 ℃, 6 h), the resulting NiFe LDH@NF composite was carefully rinsed with copious amounts of ultrapure water and ethanol to remove loosely adhered particles, then dried under a gentle N_2 stream.

1.1.4. Synthesis of ^{LSA}Mo-NiFe LDH powders

The low-valent single atom Mo-doped NiFe LDH (^{LSA}Mo-NiFe LDH) catalyst was synthesized through a solvothermal reduction method. Specifically, 2 mg of Na_2MoO_4 (99.6%, Aladdin) was first dissolved in 14 mL of 0.01 M NaOH solution (95%, Macklin), followed by the addition of 30 mg NiFe LDH powder under vigorous stirring to form a homogeneous suspension. Subsequently, 1 mL of freshly prepared 1.0 M $NaBH_4$ solution (96%, HuaWen) was slowly introduced dropwise to initiate the reduction process. The resulting mixture was then transferred to a 25 mL Teflon-lined stainless-steel autoclave and subjected to solvothermal treatment at 120 ℃ for 1 h. After natural cooling to 25 ℃, the product was collected by centrifugation (4000 rpm, 5 min), thoroughly washed with ultrapure water and ethanol (≥ 3 times each), and finally dried at 60 ℃ for 12 h to obtain the ^{LSA}Mo-NiFe LDH catalyst.

1.1.5. Synthesis of ^{LSA}Mo-NiFe LDH @NF electrode

The ^{LSA}Mo-NiFe LDH@NF electrode was fabricated *via* a sequential hydrothermal–solvothermal strategy. Initially, NiFe LDH was grown *in situ* on plasma-treated nickel foam (NF) through a facile hydrothermal process to obtain the NiFe LDH@NF electrode. Briefly, a piece of plasma-treated NF was immersed in 15 mL of precursor solution in a 25 mL Teflon-

lined stainless-steel autoclave and maintained at 120 °C for 6 h. The precursor solution was prepared by dissolving 348.9 mg of $Ni(NO_3)_2 \cdot 6H_2O$ (98%, Alfa), 79.5 mg of $FeCl_2 \cdot 4H_2O$ (99.95%, Macklin), and 296 mg of NH_4F (98%, Aladdin) in 40 mL of ultrapure water (18.2 MΩ cm) to form a homogeneous pea-green solution, followed by the addition of 480.5 mg of urea under vigorous stirring until complete dissolution. Subsequently, ^{LSA}Mo-NiFe LDH@NF was obtained by reacting the as-prepared NiFe LDH@NF electrode with 2 mg of Na_2MoO_4 in 14 mL of 0.01 M NaOH solution and 1 mL of 1.0 M $NaBH_4$ solution at 120 °C for 1 h. The final product was thoroughly washed with ultrapure water and ethanol, and then dried under a nitrogen flow.

1.2. Material Characterization

The powder X-ray diffraction (PXRD) pattern was acquired on a Bruker D8 Advance diffractometer equipped with a Cu Kα radiation source (λ = 1.5418 Å), with data collected in the 2θ range of 5–70° at a scan rate of 5° min^{-1}. Fourier-transform infrared (FT-IR) spectroscopy was performed using a Bruker VECTOR-22 spectrophotometer, covering the wavenumber range of 400–4000 cm^{-1}. Raman spectroscopic measurements were conducted on a Thermo Fisher DXR spectrometer. Morphological characterization was carried out using a Zeiss Sigma 300 scanning electron microscope (SEM) operating at an accelerating voltage of 3 kV. Transmission electron microscopy (TEM) investigations, including high-angle annular dark-field scanning TEM (HAADF-STEM) and selected-area electron diffraction (SAED), were performed using a JEOL JEM-2100F microscope. Spherical aberration-corrected HAADF-STEM imaging was additionally conducted on a JEOL JEM-ARM-200F

instrument. the high-resolution electron energy loss spectroscopy (EELS) (Spherical aberration-corrected HAADF-STEM imaging was performed using a Spectra 300 microscope (FEI, USA) at an accelerating voltage of 300 kV. In addition, high-resolution electron energy loss spectroscopy (EELS) analysis was performed on this instrument.) X-ray photoelectron spectroscopy (XPS) analysis was performed using a Thermo Scientific K-Alpha spectrometer with monochromatic Al Kα radiation (hν = 1486.6 eV). All XPS spectra were calibrated by referencing the C 1s peak at 284.6 eV. X-ray absorption near-edge spectroscopy (XANES) and extended X-ray absorption fine structure (FT-EXAFS) spectra were performed at the BL14W beamline in Shanghai Synchrotron Radiation Facility (SSRF). The synchrotron storage ring operated at an electron energy of 3.5 GeV with a stable beam current of 200 mA. A Si (311) double-crystal monochromator was used for energy selection, the spectra were collected in fluorescence mode using a Lytle detector. All measurements were conducted under ambient conditions. Athena and Artemis software packages [S1] were employed for data processing and fitting, including normalization of XANES spectra, FT-EXAFS analysis, as well as extraction of bond lengths and coordination numbers.

1.3. Electrochemical Characterization

Preparation of working electrodes: For the powder-based catalysts (^{LSA}Mo-NiFe LDH, pure NiFe LDH, and commercial IrO_2), a homogeneous ink was prepared by dispersing 5 mg of catalyst in a mixed solvent system containing 600 μL ultrapure water, 400 μL ethanol, and 20 μL Nafion solution (5wt%, Sigma-Aldrich), followed by ultrasonication for at least 30 min. A 5 μL aliquot of this suspension was then precisely drop-cast onto a polished glassy carbon

(GC) electrode, resulting in a controlled catalyst loading of approximately 130 μg cm^{-2}. The modified electrode was subsequently dried under mild infrared irradiation. The ^{LSA}Mo-NiFe LDH@NF electrode was employed directly without any additional processing. The catalyst loading on nickel foam (~ 2.04 mg cm^{-2}) was determined gravimetrically by measuring the mass difference of the nickel foam substrate before and after the *in situ* growth process.

Preparation of IrO_2/NF electrode: 5 mg of commercial IrO_2 was dispersed in a mixed solvent containing 600 μL ultrapure water, 400 μL ethanol, and 20 μL Nafion, followed by ultrasonication for at least 30 min to form a homogeneous ink. Subsequently, 416 μL of the ink was drop-cast onto a 1 cm × 1 cm nickel foam substrate, affording a catalyst loading of ~2.04 mg cm^{-2}, which is identical to that of the ^{LSA}Mo–NiFe LDH@NF electrode. The electrode was then dried under mild infrared irradiation.

Electrocatalytic measurement: All electrochemical measurements were performed using a CHI 760E electrochemical workstation in a standard three-electrode configuration with a rotating disk electrode (RDE, Pine Research Instrument) system. The working electrode consisted of a polished glassy carbon electrode (GC, AFE5T050GC, 5 mm diameter, 0.196 cm^2 geometric area), while a Pt wire and Hg/HgO (1 M KOH) electrode served as the counter and reference electrodes, respectively. All potentials were converted to the reversible hydrogen electrode (RHE) scale using the Nernst equation: $E_{RHE} = E_{Hg/HgO} + 0.059 \times pH + 0.098$ V. For 1.0 M KOH electrolyte (pH ~13.97, determined by averaging at least three measurements using a PHS-3E pH meter), the conversion equation became $E_{RHE} = E_{Hg/HgO} + 0.922$ V. The electrolyte was continuously purged with high-purity oxygen (99.999%) during

OER measurements. Cyclic voltammetry (CV) and linear sweep voltammetry (LSV) were performed between 0.2 – 0.8 V (*vs*. Hg/HgO) at a scan rate of 5 mV s^{-1}, with all polarization curves manually *i*R-compensated at 95% (Figure S6). Electrochemical impedance spectroscopy (EIS) was conducted at 0.55 V (*vs*. Hg/HgO) over a frequency range of 480 Hz to 1 kHz. The electrochemical active surface area (ECSA) was evaluated through double-layer capacitance (C_{dl}) measurements in the non-faradaic potential region (0.2–0.3 V *vs*. Hg/HgO) at varying scan rates (20–100 mV s^{-1}).[S2] The C_{dl} was obtained from the slope of $\Delta j = (j_a - j_c)/2$ at 0.25 V *versus* scan rate. ECSA was calculated using [S3,S4]: $ECSA = C_{dl}/C_s$, where C_s represents the specific capacitance of the bare GC electrode (163.8 μF cm^{-2}, averaged from three independent measurements). The normalized CVs enabled direct comparison of intrinsic OER activities among different catalysts. Galvanostatic stability tests were performed at 10 mA cm^{-2} for 12 and 85 h durations. To investigate the OER kinetics of the ^{LSA}Mo-NiFe LDH, CV was performed in a potential window of 0.2–0.8 V (*vs*. Hg/HgO) at 5 mV s^{-1}, with the electrode rotating at 1600 rpm. During these measurements, the Pt ring electrode was maintained at a constant potential 1.50 V (*vs.* RHE) to monitor potential reaction intermediates. The electron transfer number (N), which reflects the formation of HO_2^- species at the Pt ring electrode during OER, was determined using Equation 1[S5]. The Faradaic efficiency (FE) was evaluated through chronoamperometric measurements conducted for 100 s in N_2-saturated 1.0 M KOH electrolyte, with the Pt ring electrode held at 0.4 V (*vs*. RHE) to ensure complete reduction of any evolved oxygen. The FE value was calculated according to Equation 2 [S6], providing quantitative assessment of the charge

utilization efficiency for oxygen evolution.

$$N = \frac{4I_d}{I_d + I_r/N_{CL}} \quad \text{(Equation 1)}$$

$$FE = \left|\frac{I_r n_d}{I_d n_r N_{CL}}\right| \quad \text{(Equation 2)}$$

where I_r and I_d represent ring and disk currents, n_d (4) and n_r (2) are electron transfer numbers for disk ($4OH^- \rightarrow O_2 + 2H_2O + 4e^-$) and ring ($O_2 + 2H_2O + 2e^- \rightarrow 2OH^-$) reactions, respectively, and N_{CL} (0.37) is the collection efficiency.

Turnover frequencies (TOFs) were calculated using Equation (3) [S7,S8], where *j* is the current density at an overpotential of 300 mV (A cm^{-2}), N_A is Avogadro′s number, F is the Faraday constant (96485 C mol^{-1}), n is the number of electrons transferred per molecule of product (for O_2 generation in the OER, n = 4), and Γ represents the number of surface active sites in the catalyst. Γ was determined from Equation (4), in which *Q* is the total charge associated with the redox-active sites, *z* is the number of electrons transferred per site, and *e* is the elementary charge (1.6×10^{-19} C). Polarization curves (Figure 3a) were recorded at 5 mV s^{-1} and display reversible Ni^{3+}/Ni^{2+} redox peaks. Based on literature reports, Ni^{3+} species were considered the active sites for OER; thus, $z = 1$. The charge (*Q*) was obtained from the integrated area (*S*) of the Ni^{3+}/Ni^{2+} redox peak divided by the scan rate (*v*), as defined in Equation (5). Here, *S* was obtained by integrating the Ni^{3+}/Ni^{2+} redox peak (Table S4), and *v* = 5 mV s^{-1}.

$$TOF = \frac{j \times N_A}{n \times F \times \Gamma} \quad \text{(Equation 3)}$$

$$\Gamma = \frac{Q}{z \times e} \quad \text{(Equation 4)}$$

$$Q = \frac{S}{v} \quad \text{(Equation 5)}$$

Operando attenuated total reflectance surface-enhanced infrared absorption spectroscopy (ATR-SEIRAS): *Operando* ATR-SEIRAS spectra were acquired using a Thermo Nicolet NEXUS 470 spectrometer equipped with a liquid nitrogen-cooled mid-wavelength MCT detector (A530/P controller) and controlled *via* OPUS software. Spectra were collected at 8 cm^{-1} resolution with 27 cumulative scans, using a grating setting of 1.5 mm for optimal signal detection. The experiments were performed in a three-electrode electrochemical cell containing 1 M KOH electrolyte, with a Hg/HgO reference electrode, a Pt sheet counter electrode, and a working electrode prepared by drop-coating the catalyst onto a gold-plated silicon ATR prism. Prior to catalyst deposition, the gold-coated silicon prisms were mechanically polished with 0.05 μm Al_2O_3 powder and thoroughly cleaned *via* alternating rinses with deionized water and acetone to ensure a contaminant-free surface.

Operando differential electrochemical mass spectrometry (DEMS) with isotope labelling experiments: Operando DEMS coupled with ^{18}O isotope labelling were performed using a QAS 100 system (LingLu Instruments, Shanghai) featuring a dual-chamber configuration. The setup comprised a high-vacuum chamber housing a quadrupole mass spectrometer and an ambient-pressure electrochemical cell chamber. Experiments were conducted in argon-saturated 1.0 M KOH using a three-electrode system with Pt wire counter electrode and Ag/AgCl (saturated KCl) reference electrode. The working electrode was prepared by uniformly depositing ^{LSA}Mo-NiFe LDH catalyst ink (1 mg cm^{-2} loading) on 1 cm^2 carbon paper (0.21 cm^2 active area), encapsulated with PTFE membranes for selective gas permeation while preventing electrolyte leakage. For isotope tracing, the

catalyst was first cycled (20 CVs, 1.1–1.7 V *vs.* RHE, 5 $mV \cdot s^{-1}$) in ^{18}O-enriched KOH electrolyte, followed by thorough washing with ^{16}O water to remove physisorbed $H_2{}^{18}O$. Subsequent LSV measurement (5 cycles) in normal ^{16}O-based electrolyte enabled real-time MS monitoring of oxygen isotopologues ($^{32}O_2$, $^{34}O_2$, and $^{36}O_2$) evolution during OER. Continuous argon purging (99.999%) maintained oxygen-free conditions throughout experiments.

1.4. Theoretical calculations

All DFT calculations were conducted in the Vienna Ab initio Simulation Package (VASP) with a cutoff energy of 400 eV for plane-wave basis set.[S9] The exchange correlation function for the valence electrons was employed by Perdew–Burke–Ernzerhof (PBE) within the generalized gradient approximation (GGA).[S10] A Hubbard with U correction was used to describe better d-electrons cross-correlation effect of Ni and Fe in ^{LSA}Mo/NiFe LDH and pure NiFe LDH catalysts. According to the previous literature reports, the U values of 6.2 and 5.3 eV for Ni and Fe atoms, respectively.[S11]–[S13] The Brillouin zone of supercells (3 × 3 × 3) was sampled by a 5 × 5 × 1 Monkhorst-Pack k-point mesh. The models were completely optimized via the convergence criteria of at least 10^{-6} eV for the electronic energy and at lowest 0.05 eV/Å for the forces on per atom.

2. Additional Data and Figures

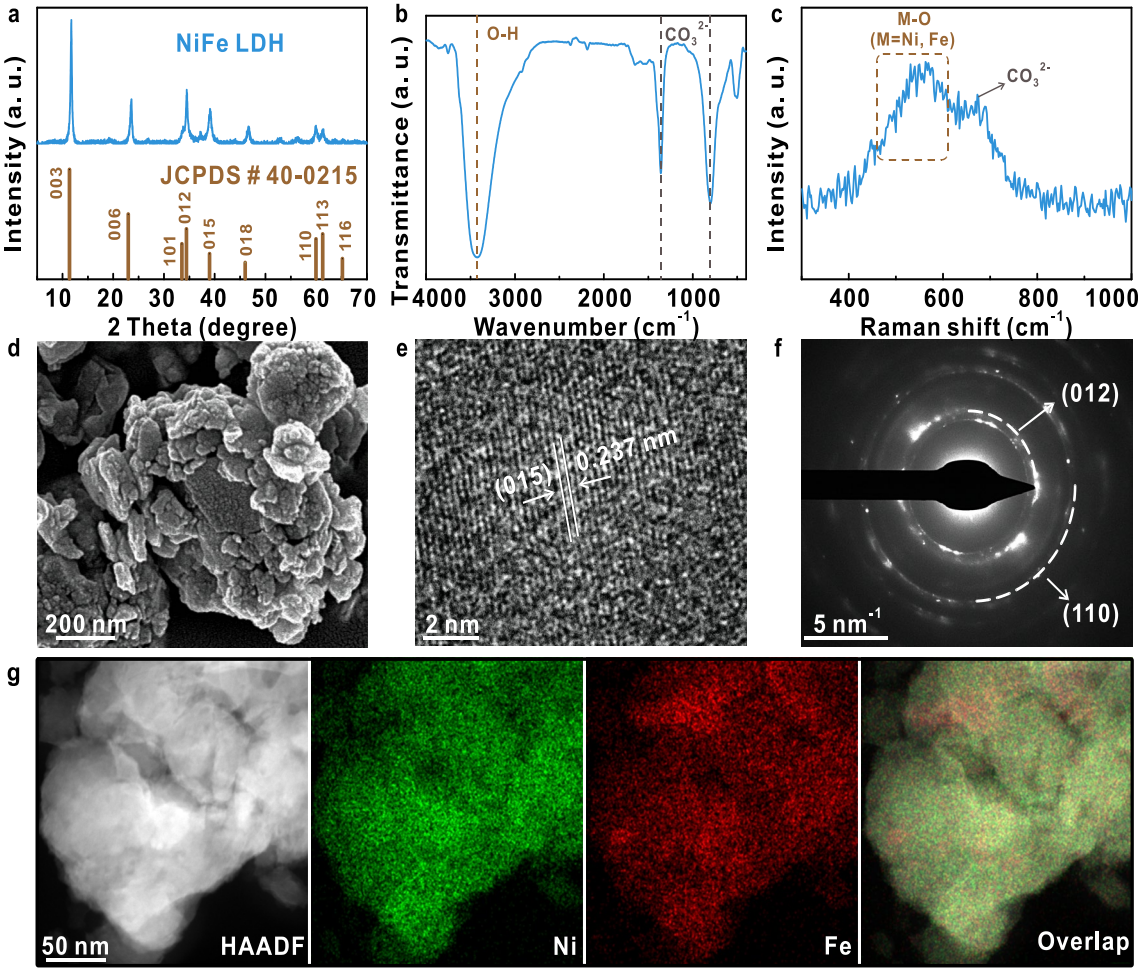

Figure S1. Material characterization of NiFe LDH powders. (a) PXRD pattern. (b) FT-IR spectrum. (c) Raman spectrum. (d) SEM image. (e) High-resolution TEM image. (h) SAED pattern. (g) HAADF-STEM image and corresponding elemental distribution maps.

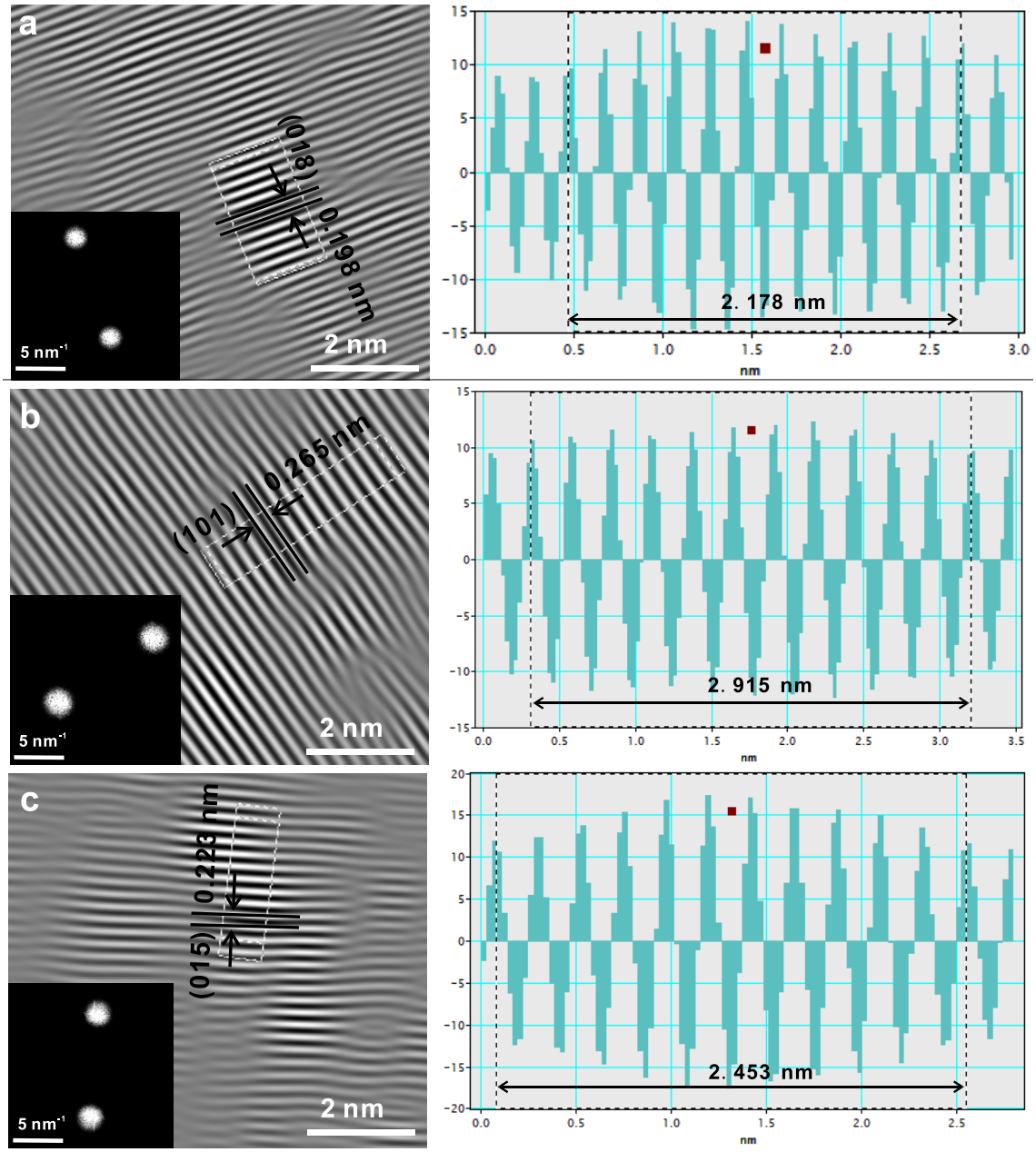

Figure S2. HRTEM images of ^{LSA}Mo-NiFe LDH powder, showing the fast-Fourier transform (FFT) patterns of different crystal planes (illustrated in the left inset), inverse FFT (IFFT) patterns (left image), and corresponding interplanar spacing images (right image). (a) (018) plane, (b) (101) plane, (c) (015) plane.

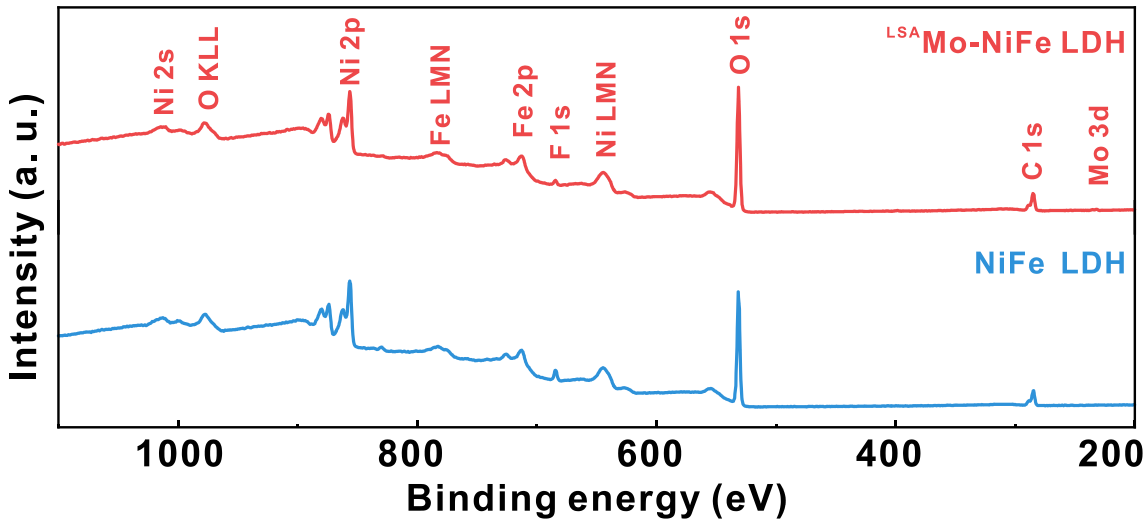

Figure S3. XPS survey spectra of two LDH powders.

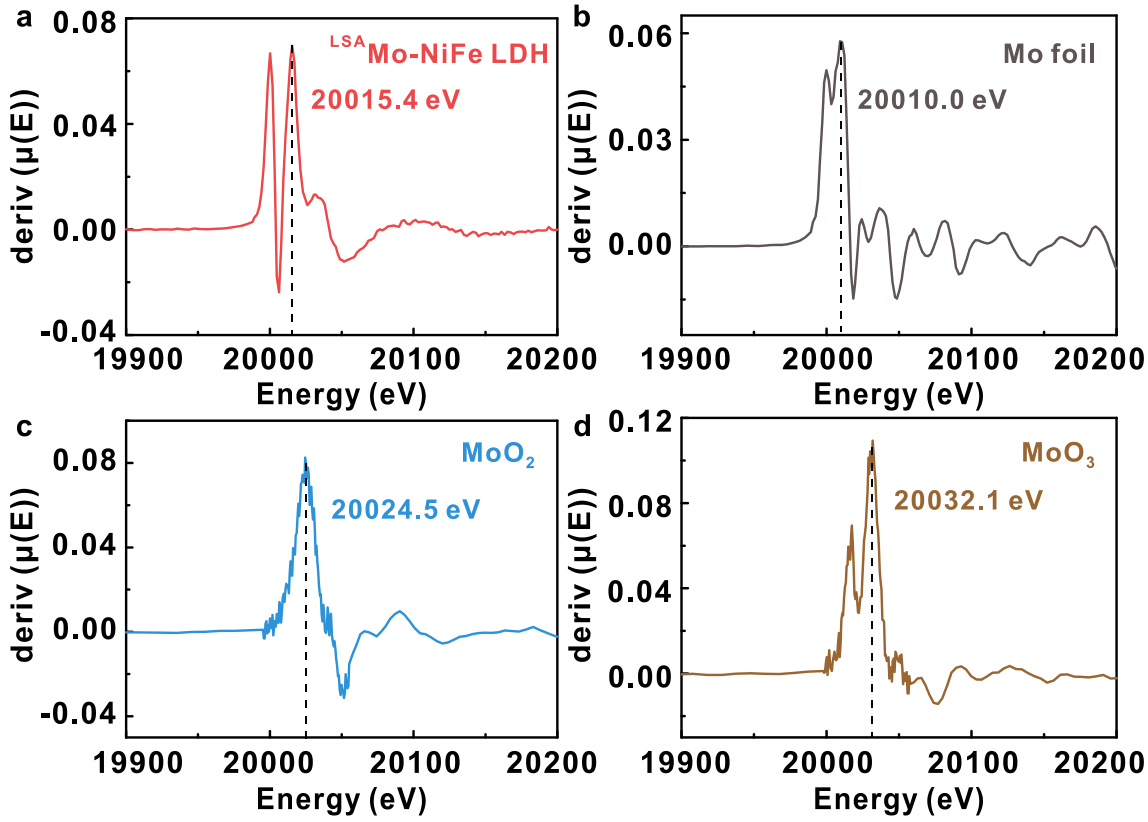

Figure S4. The first derivative curves of the XANES spectra of (a) ^{LSA}Mo-NiFe LDH, (b) Mo foil, (c) MoO_2, and (d) MoO_3.

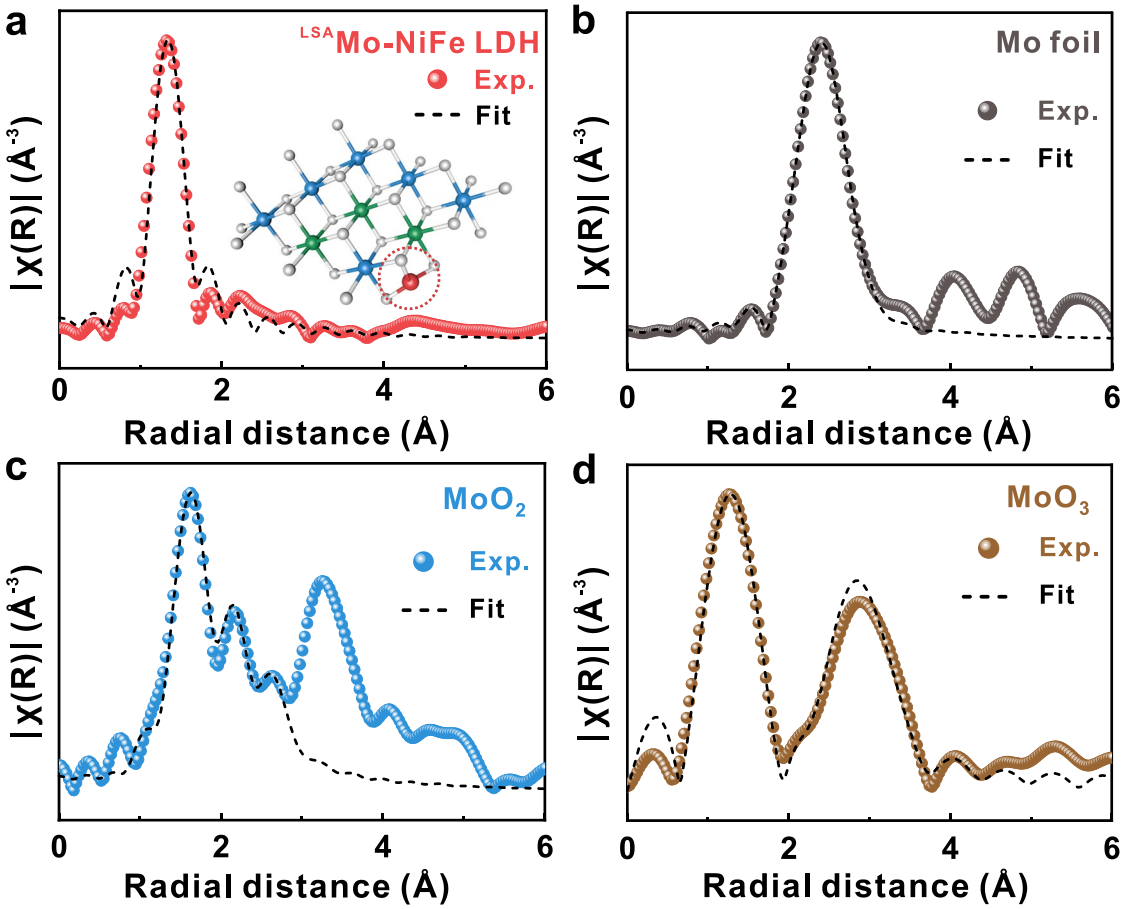

Figure S5. (a) Valence states of different molybdenum samples obtained from Mo k-edge XANES. EXAFS R-space fitting of (b) Mo foil, (c) MoO_2, (d) MoO_3.

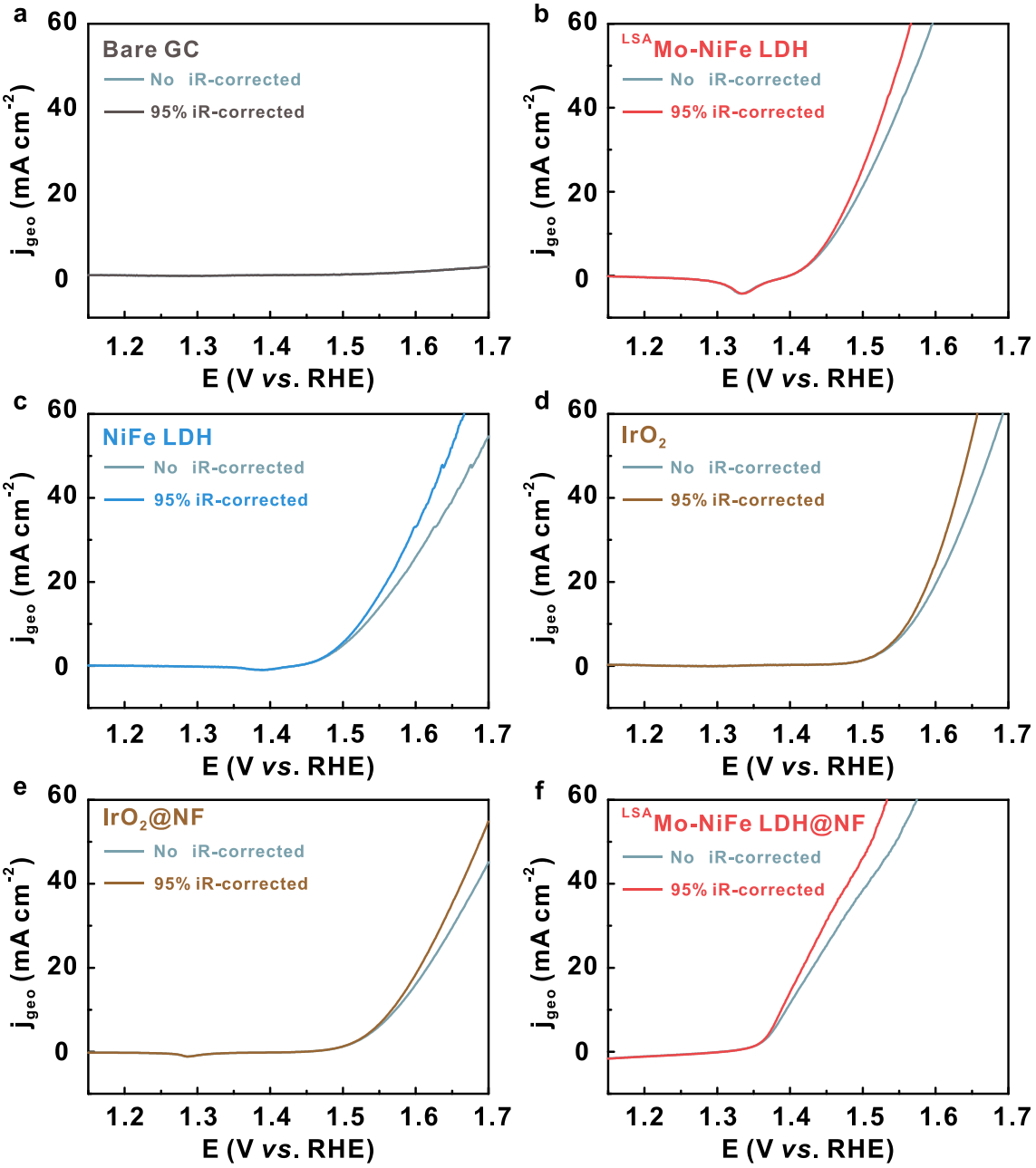

Figure S6. Polarization curves of all modified glassy carbon and nickel foam electrodes with and without 95% *i*R correction in O_2-purged 1.0 M KOH media.

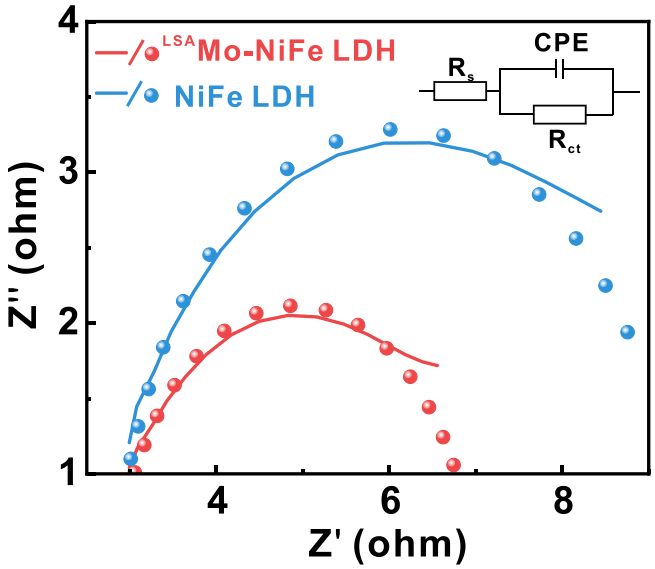

Figure S7. Electrochemical impedance spectroscopy (EIS) with fitting of ^{LSA}Mo-NiFe LDH and pristine NiFe LDH samples. The inset is the corresponding equivalent circuit. Circles and lines stand for the experimental and fitted data, respectively.

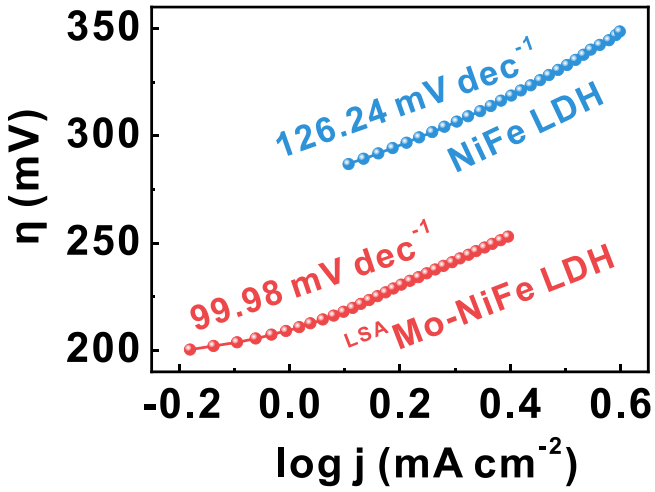

Figure S8. Tafel plots of ^{LSA}Mo-NiFe LDH and pure NiFe LDH samples normalized by electrochemically active surface area (ECSA).

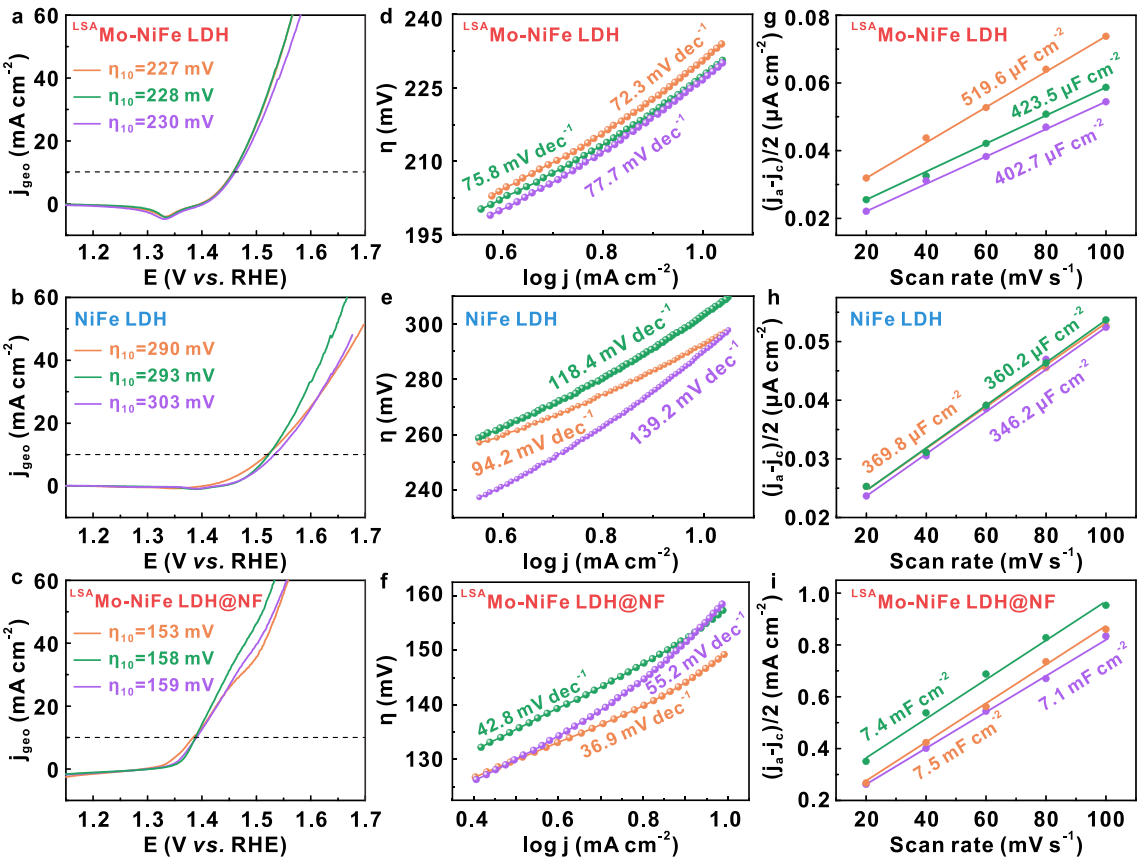

Figure S9. Three independent electrochemical tests of ^{LSA}Mo-NiFe LDH, NiFe LDH and ^{LSA}Mo-NiFe LDH@NF (a, b, c) LSV curves, (d, e, f) Tafel slopes, (g, h, i) C_{dl}.

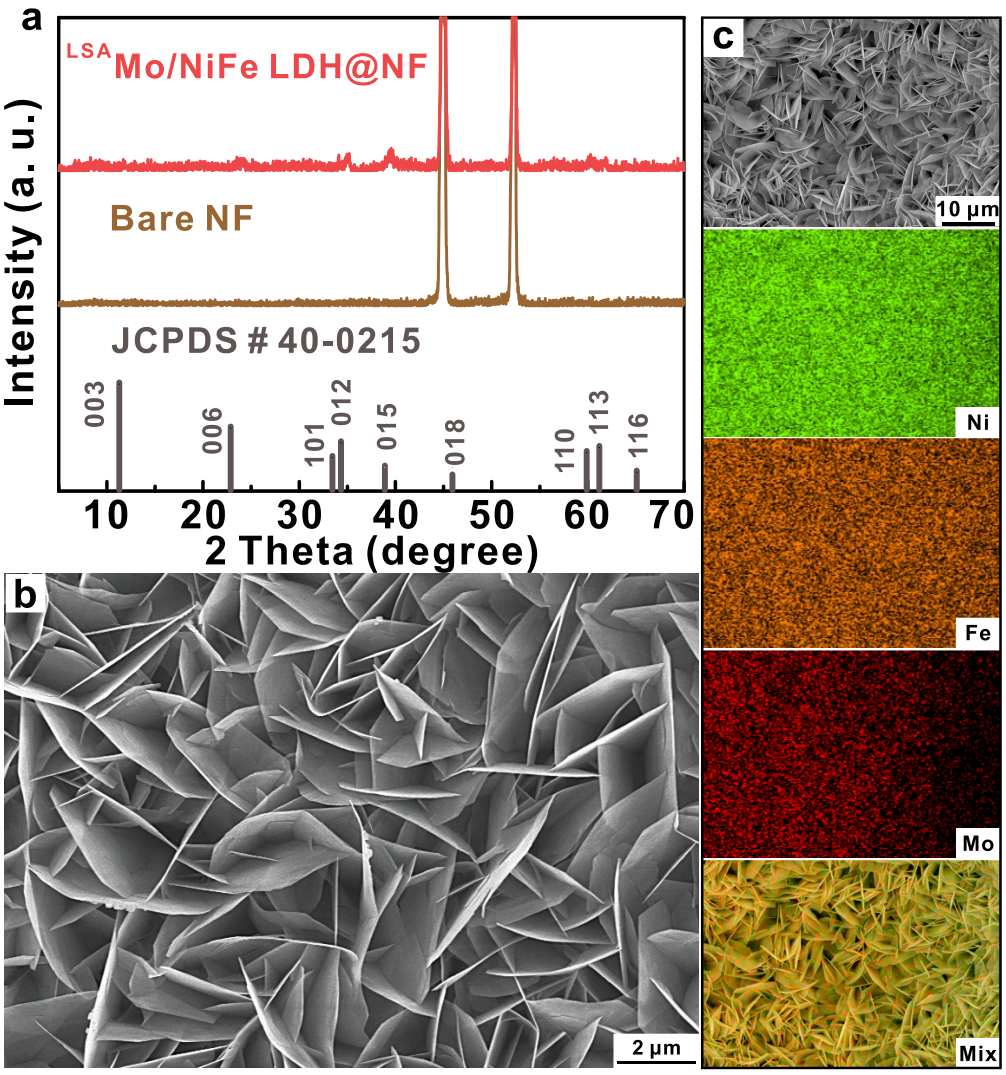

Figure S10. (a) XRD patterns of nickel foam and ^{LSA}Mo-NiFe LDH@NF. (b) SEM image and (c) Elemental maps of ^{LSA}Mo-NiFe LDH@NF.

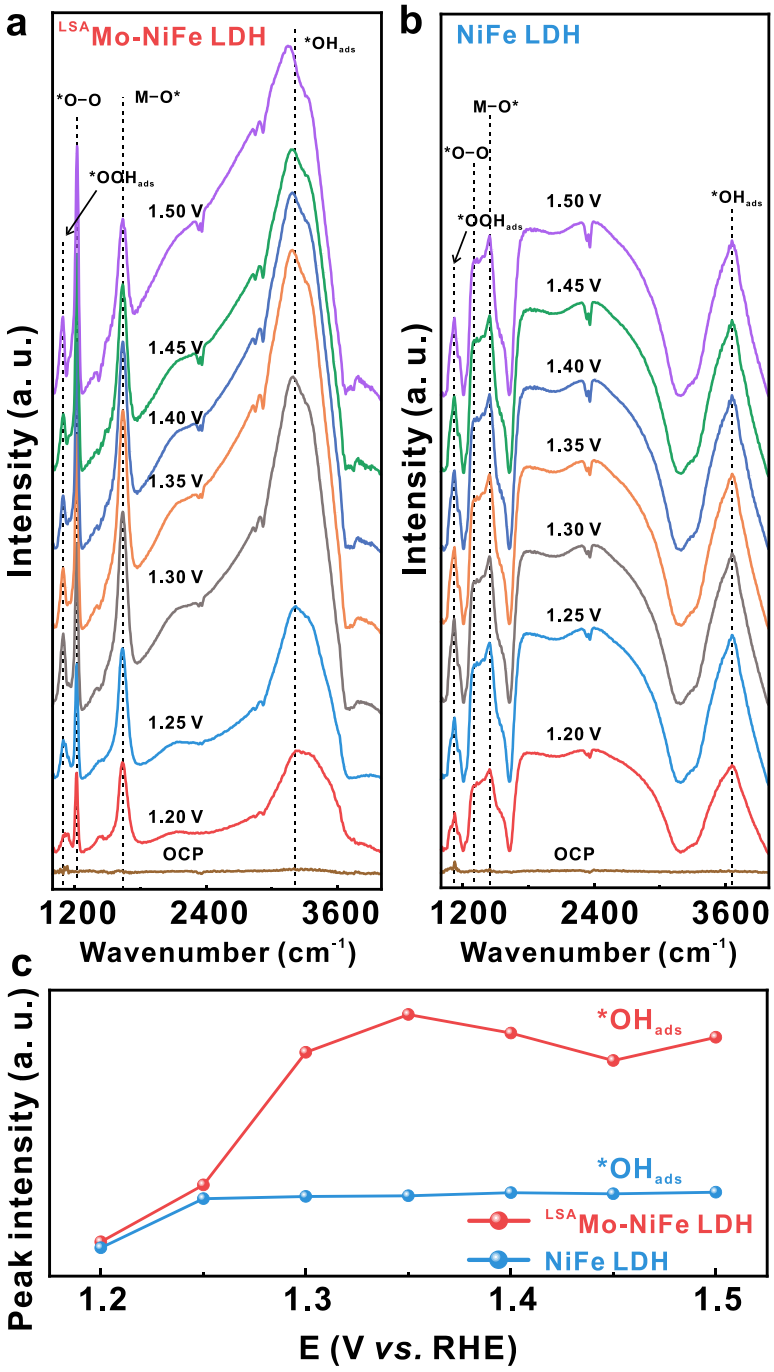

Figure S11. OER pathway over a ^{LSA}Mo-NiFe LDH catalyst *via operando* electrochemical characterizations. *Operando* ATR-SEIRAS spectra at different applied potentials for (a) ^{LSA}Mo-NiFe LDH and (b) pristine NiFe LDH. (c) The intensities of $^{*}OH_{ads}$ intermediates at a potential range of 1.2 to 1.5 V (*vs.* RHE).

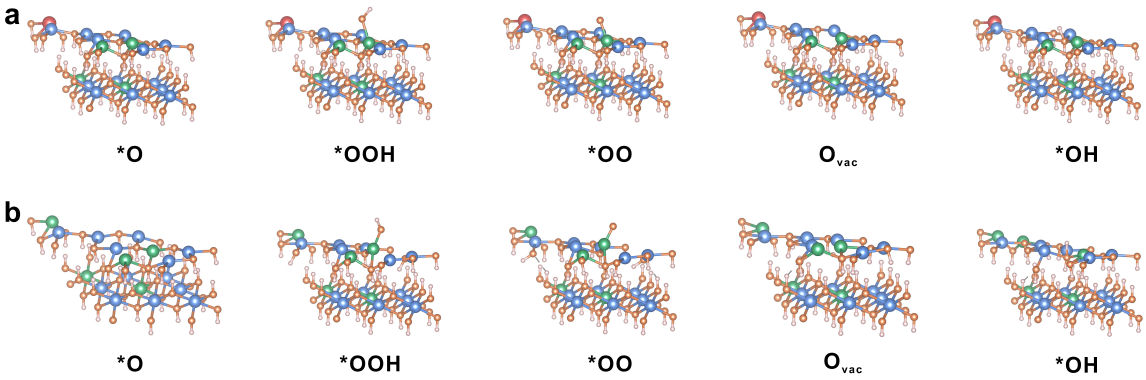

Figure S12. Adsorption models for LOM pathway on (a) ^{LSA}Mo-NiFe LDH and (b) pristine NiFe LDH catalysts.

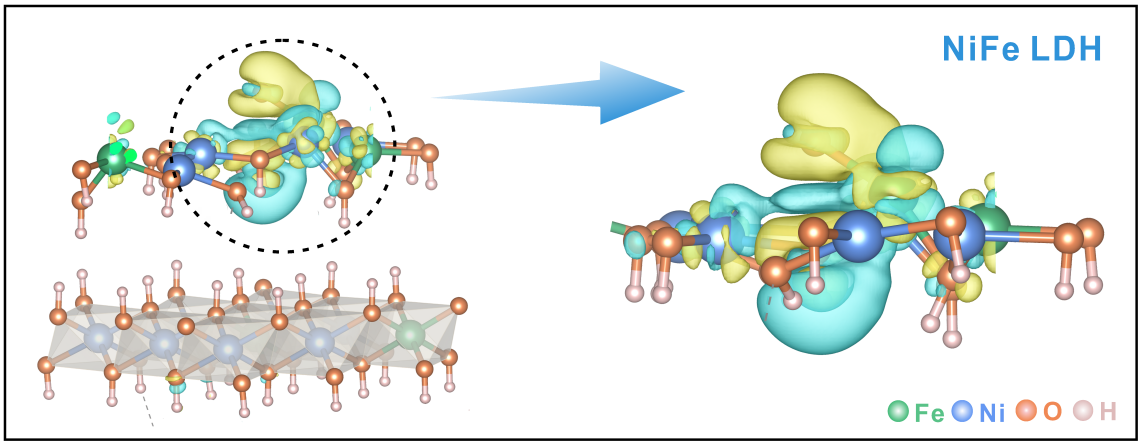

Figure S13. Differential charge densities of pristine NiFe LDH. Chrome yellow and cyan contour lines represent the electron gain and loss, respectively. The isosurface level is set as 0.011 e/Bohr^3.

Table S1. Quantitative XPS analysis data of ^{LSA}Mo-NiFe LDH powder.

Elements	Atomic content (%)	Mass (%)
Ni 2p	15.98	36.72
Fe 2p	8.74	19.16
O 1s	52.51	32.90
C 1s	22.61	10.61
Mo 3d	0.16	0.61

Table S2. Fitting parameters of ^{LSA}Mo-NiFe LDH catalyst under EXAFS spectra (C.N: coordination number; R: bond distance; E_0: energy shift; R factor: goodness or fit).

Catalyst	Path	C.N	R(Å)	E_0(eV)	R factor
Mo foil	Mo-Mo	6.96± 0.61	2.71	-7.944	0.00125
		5.50± 1.08	3.12		
MoO_2	Mo-O	4.20± 0.20	2.02	3.598	0.02050
	Mo-Mo	1.78± 0.32	2.80		
		1.46± 0.19	2.59		
MoO_3	Mo-O	2.02± 0.13	1.85	7.885	0.02008
	Mo-Mo	1.65± 0.26	3.03		
		3.62± 0.38	2.95		
^{LSA}Mo-NiFe LDH	Mo-O	2.85± 0.53	1.78	-0.444	0.01654

Table S3. EIS fitting parameters of two LDHs.

	^{LSA}Mo-NiFe LDH	NiFe LDH
R_{ct} (Ω)	4.228	6.568
R_s (Ω)	2.8	2.359
CPE (F)	0.3193×10^{-6}	0.2502×10^{-6}

Table S4. The Ni^{3+}/Ni^{2+} redox peak areas of ^{LSA}Mo-NiFe LDH and pristine NiFe LDH.

Catalysts	Ni^{3+}/Ni^{2+} redox peak areas (V·A)
^{LSA}Mo-NiFe LDH	4.48×10^{-5}
NiFe LDH	2.27×10^{-5}

Table S5. Comparison of the catalytic activity and performance of ^{LSA}Mo-NiFe LDH and a recently reported base metal combined with LDH catalyst in 1.0 M KOH media.

Catalysts	j ($mA\ cm^{-2}$)	η (mV)	Tafel slope ($mV\ dec^{-1}$)	Ref.
^{LSA}Mo-NiFe LDH	10	228	75.8	This work
^{s}Au/NiFe LDH	10	237	36	[S14]
$NiFeMo(OH)_2$	10	236	44	[S15]
Mo-NiFe LDH	10	290	44	[S16]
Mo-CoOOH	10	249	60.5	[S17]
^{LSA}Mo-NiFe LDH/NF	10	158	42.8	This work
$CoMn_2$Mo-LDH/NF	10	242	87.61	[S18]
MoNiFe/NF	10	205	31.7	[S19]
Ru/NiFe LDH-F/NF	10	230	50.2	[S20]
CoMo-LDH/NF	10	300	56	[S21]
Mo-NiS_x@NiFe LDH/NF	10	224	44.41	[S22]
NiFe LDH@NiCoP/NF	10	220	48.6	[S23]

Table S6. Quantitative XPS analysis data before and after stability test of ^{LSA}Mo-NiFe LDH@NF electrode

Elements		Before	After
Ni 2p	Ni $2p_{3/2}$	277.17	184.76
	Ni $2p_{1/2}$	98.39	50.08
Fe 2p	Fe $2p_{3/2}$	145.49	90.95
	Fe $2p_{1/2}$	48.89	26.41
Mo 3d	Mo $3d_{5/2}$	1.71	0.75
	Mo $3d_{3/2}$	4.11	1.05
		0	0.66

Reference

[S1] Ravel, B.; Newville, M. Athena, Artemis, Hephaestus: data analysis for X-ray absorption spectroscopy using IFEFFIT. *J. Synchrotron Radiat.,* **2005,** 12(4), 537–541. https://doi.org/10.1107/S0909049505012719.

[S2] Y. S. Park, W-S. Choi, M. J. Jang, J. H. Lee, S. Park, H. Jin, M. H. Seo, K-H. Lee, Y. Yin, Y. Kim, J. Yang and S. M. Choi, Three-dimensional dendritic Cu-Co-P electrode by one-step electrodeposition on a hydrogen bubble template for hydrogen evolution

reaction. *ACS. Sustainable. Chem. Eng.,* **2019**, 7, 10734-10741. https://doi.org/10.1021/acssuschemeng.9b01426.

[S3] S. N. Sun, H. Y. Li, Z. C. J. Xu, Impact of surface area in evaluation of catalyst activity. *Joule.,* **2018**, 2, 1024−1027. https://doi.org/10.1016/j.joule.2018.05.003.

[S4] J. T. Li, W. Z. Huang, M. M. Wang, S. B. Xi, J. S. Meng, K. N. Zhao, J. Jin, W. W. Xu, Z. Y. Wang, X. Liu, Q. Chen, L.H. Xu, X. B. Liao, Y. L. Jiang, K. A. Owusu, B. L. Jiang, C. X. Chen, D. N. Fan, L. Zhou, L. Q. Mai, Low-crystalline bimetallic metal-organic framework electrocatalysts with rich active sites for oxygen evolution. *ACS. Energy. Lett.,* **2019,** 4, 285−292. https://doi.org/10.1021/acsenergylett.8b02345.

[S5] X. H. Zhao, B. Pattengale, D. H. Fan, Z. H. Zou, Y. Q. Zhao, J. Du, J. E. Huang, and C. L. Xu, Mixed-node metal-organic frameworks as efficient electrocatalysts for oxygen evolution reaction. *ACS. Energy. Lett.,* **2018**, 3, 2520-2526. https://doi.org/10.1021/acsenergylett.8b01540.

[S6] Y. S. Zhao, N. L. Yang, H. Y. Yao, D. B. Liu, L. Song, J. Zhu, S. Z. Li, L. Gu, K. F. Lin, D. Wang, Stereodefined codoping of sp-N and S atoms in few-layer graphdiyne for oxygen evolution reaction. *J. Am. Chem. Soc.,* **2019**, 141, 7240-7244. https://doi.org/10.1021/jacs.8b13695.

[S7] L. Zhang, Y. X. Zhu, Z. C. Nie, Z. Y. Li, Y. Ye, L. H. Li, J. Hong, Y. T. Zhou, G. Z. Hu, Co/MoC nanoparticles embedded in carbon nanoboxes as robust trifunctional electrocatalysts for a Zn–air battery and water electrocatalysis. *ACS Nano.,* **2021,** 15(8): 13399-13414. https://doi.org/10.1021/acsnano.1c03766.

[S8] S. Anantharaj, S. R. Ede, K. Karthick, S. Sam Sankar, K. Sangeetha, P. E. Karthik, S. Kundu, Precision and correctness in the evaluation of electrocatalytic water splitting: revisiting activity parameters with a critical assessment. *Energy Environ. Sci.,* **2018,** 11(4): 744-771. https://doi.org/10.1039/C7EE03457A.

[S9] G. Kresse, J. Furthmüller, Efficient iterative schemes for ab initio total-energy calculations using a plane-wave basis set. *Phys. Rev. B.,* **1996**, 54, 11169−11186. https://doi.org/10.1103/PhysRevB.54.11169.

[S10] J. P. Perdew, K. Burke, M. Ernzerhof, Generalized gradient approximation made simple. *Phys. Rev. Lett.,* **1996***,* 77, 3865−3868. https://doi.org/10.1103/PhysRevLett.77.3865.

[S11] S. L. Dudarev, G. A. Bottom, S. Y. Savrasov, C. J. Humphreys, A. P. Sutton, Electron-energy-loss spectra and the structural stability of nickel oxide: an LSDA+U study. *Phys. Rev. B.,* **1998***,* 57, 1505−1509. https://doi.org/10.1103/PhysRevB.57.1505.

[S12] M. P. J. Punkkinen, K. Kokko, W. Hergert, I. J. Väyrynen, Fe_2O_3 within the LSDA+U approach. *J. Phys. Condens. Matter.,* **1999,** *11,* No. 2341. https://doi.org/10.1088/0953-8984/11/11/006.

[S13] P. F. Guo, Y. Yang, W. J. Wang, B. Zhu, W. T. Wang, Z. Y. Wang. J. L. Wang, K. Wang, Z H. He, Z. T. Liu, Stable and active NiFeW layered double hydroxide for enhanced electrocatalytic oxygen evolution reaction. *Chem. Eng. J.,* **2021**, 426, No. 130768. https://doi.org/10.1016/j.cej.2021.130768.

[S14] J. F. Zhang, J. Y. Liu, L. F. Xi, Y. F. Yu, N. Chen, S. H. Sun, W. C. Wang, K. M.

Lange, B. Z. Zhang, Single-atom Au/NiFe layered double hydroxide electrocatalyst: probing the origin of activity for oxygen evolution reaction. *J. Am. Chem. Soc.,* **2018**, 140, 3876-3879. https://doi.org/10.1021/jacs.8b00752.

[S15] J. Y. Wang, Z. Y. Xing, R. Y. Kang, Y. J. Zheng, Z. Zhang, T. Ma, Y. Wang, B. Yin,Y. Z. Liao, L. Li, C. Cheng, S. Li, Metal nitride controlled atomic doping of Mo^{x+} in NiFe (Oxy)hydroxide to trigger lattice oxygen-mediated mechanism for superior oxygen evolution. *Adv. Funct. Mater.,* **2024**, 26, 2418439. https://doi.org/10.1002/adfm.202418439.

[S16] Z. H. Yin, X. Liu, M. Cui, Z. Y. Cao, A. M. Liu, L. G. Gao, T. L. Ma, S. R. Chen, Y. Q. Li, Template synthesis of molybdenum-doped NiFe-layered double hydroxide nanotube as high efficiency electrocatalyst for oxygen evolution reaction. *Mater. Today. Sustain.,* **2022**, 17, No. 100101. https://doi.org/10.1016/j.mtsust.2021.100101.

[S17] L. Tang, L. Yu, C. Ma, Y. Song, Y. C. Tu, Y. L. Zhang, X. Bo, D. H. Deng, Three-dimensional CoOOH nanoframes confining high-density Mo single atoms for large-current-density oxygen evolution. *J. Mater. Chem. A.,* **2022**, 10, 6242-6250. https://doi.org/10.1039/d1ta09729f.

[S18] H. Zhu, Q. K. Wu, X. L. Yu, D. K. Zhao, W. Zhou, N. Wang, T. T. Hou, L. G. Li, Mo-doped cobalt-manganese layered double hydroxide for oxygen evolution reaction. *Materials. Letters.,* **2023**, 342, 134333. https://doi.org/10.1016/j.matlet.2023.134333.

[S19] J. K. Qu, Y. C. Dong, T. Zhang, C. Zhao, L. T. Wei, X. J. Guan, Impact of imetallic synergies on Mo-doping NiFeOOH: Insights into enhanced OER activity and

reconstructed electronic structure. *Front. Energy,* **2024**, 18, 850–862. https://doi.org/10.1007/s11708-024-0960-6.

[S20] Y. Wang, P. Zheng, M. X. Li, Y. R. Li, X. Zhang, J. Chen, X. Fang, Y. J. Liu, X. L. Yuan, X. P. Dai, H. Wang, Interfacial synergy between dispersed Ru sub-nanoclusters and porous NiFe layered double hydroxide on accelerated overall water splitting by intermediate modulation. *Nanoscale,* **2020**, 12, 9669-9679. https://doi.org/10.1039/d0nr01491e.

[S21] J. Bao, Z. L. Wang, J. F. Xie, L. Xu, F. C. Lei, M. L. Guan, Y. P. Huang, Y. Zhao, J. X. Xia, H. M. Li, The CoMo-LDH ultrathin nanosheet as a highly active and bifunctional electrocatalyst for overall water splitting. *Inorg. Chem. Front., **2018**,* 5, 2964-2970. https://doi.org/10.1039/c8qi00867a.

[S22] Y. Y. Li, Y. Zhang, H. T. Zhang, J. Y. Zhao, R. Song, Hollow Mo-doped NiSx nanoarrays decorated with NiFe layered double-hydroxides for efficient and stable overall water splitting. *J. Mater. Chem. A,* **2022**, 10, 18989-18999. https://doi.org/10.1039/d2ta04963e.

[S23] Z. C. Wang, S. Zeng, W. H. Liu, X. W. Wang, Q. W. Li, Z. G. Zhao, F. X. Geng, Coupling molecularly ultrathin sheets of NiFe-layered double hydroxide on $NiCo_2O_4$ nanowire arrays for highly efficient overall water-splitting activity. *ACS. Appl. Mater. Interfaces,* **2017**, 9, 1488-1495. https://doi.org/10.1021/acsami.6b13075.